# Crystal chemistry and thermoelectric transport of layered $AM_2X_2$ compounds



| | |
|---|---|
| Journal: | *Inorganic Chemistry Frontiers* |
| Manuscript ID | QI-REV-12-2017-000813.R1 |
| Article Type: | Review Article |
| Date Submitted by the Author: | 06-Mar-2018 |
| Complete List of Authors: | Peng, Wanyue ; Michigan State University, Department of Chemical Engineering and Materials Science<br>Chanakian, Sevan; Michigan State University, Department of Chemical Engineering and Materials Science<br>Zevalkink, Alexandra; Michigan State University, Chemical engineering and materials science |
| | |

Journal Name

ARTICLE TYPE

Cite this: DOI: 10.1039/xxxxxxxxxx

# Crystal chemistry and thermoelectric transport of layered $AM_2X_2$ compounds

Wanyue Peng, Sevan Chanakian, and Alexandra Zevalkink

Received Date
Accepted Date

DOI: 10.1039/xxxxxxxxxx

www.rsc.org/journalname

Compounds that crystallize in the layered $CaAl_2Si_2$ structural pattern have rapidly emerged as an exciting class of thermoelectric material with attractive $n$- and $p$-type properties. The more than 100 $AM_2X_2$ compounds that form this structure type - characterized by anionic $M_2X_2$ slabs sandwiched between layers of octahedrally coordinated $A$ cations - provide numerous potential paths to chemically tune every aspect of thermoelectric transport. This review highlights the chemical diversity of this structure type, discusses the rules governing its formation and stability relative to competing $AM_2X_2$ structures (e.g., $ThCr_2Si_2$ and $BaCu_2S_2$), and attempts to bring some of the most recently discovered compounds into the spotlight. The discussion of thermoelectric transport properties in $AM_2X_2$ compounds focuses primarily on the intrinsic parameters that determine the *potential* for a high figure of merit: the band gap, effective mass, degeneracy, carrier relaxation time, and lattice thermal conductivity. We also discuss routes that have been used to successfully control the carrier concentration, including controlling the cation vacancy concentration, doping, and isoelectronic alloying (approaches that are, in reality, highly interdependent). Finally, we discuss recent progress made towards $n$-type doping in this system, highlight opportunities for further improvements, as well as open questions that still remain.

## 1 Introduction

Thermoelectric materials, which can be used to convert a temperature gradient into electricity, have applications ranging from recovering energy from waste heat in industrial or automotive settings, to powering small remote sensors and large scale space exploration missions[1]. The thermoelectric conversion efficiency of a given material is directly correlated to its figure of merit, $zT = \frac{\sigma\alpha^2 T}{\kappa}$, necessitating materials with high Seebeck coefficients ($\alpha$), high electrical conductivity ($\sigma$), low thermal conductivity ($\kappa$), and excellent thermal and chemical stability at high temperature, $T$. This requirement is not easily achieved as $\alpha$, $\sigma$, and $\kappa$ are highly interdependent[2]. The contradictory requirements of high $\sigma$ and high $\alpha$ require semiconductors with highly mobile carriers and simultaneously high electronic density of states at the band edge. At the same time, the need for high $\sigma$ conflicts with the requirement of low, glass-like lattice thermal conductivity.

The best thermoelectric materials known today succeed in this balancing act by combining light carrier effective mass, high band degeneracy, small deformation potentials (reduced electron-phonon scattering), and either complex unit cells or strongly anharmonic bonding, or both[3,4]. Zintl phases - one successful class of thermoelectrics - can be broadly defined as a subset of intermetallic phases comprised of polyanionic frameworks with electropositive cations providing overall charge balance[5,6]. A growing number of Zintl phases have succeeded as thermoelectric materials, primarily on the basis of their structural complexity, low lattice thermal conductivity, and their excellent stability at high temperature (i.e., they benefit from the $T$ in $zT$)[7–12]. For example, the heavily-doped Zintl phase $Yb_{14}MnSb_{11}$ has extremely low, temperature-independent lattice thermal conductivity, a peak $zT$ of 1.3 at 1273 K, and has been shown to be stable during life-time testing for over 1500 hours at 1273 K[13], making it the best known high-temperature $p$-type thermoelectric material. Other Zintl phases exhibit a high ratio of electronic mobility to lattice thermal conductivity, making them ideal electron-crystal, phonon-glass materials[8,11].

In recent years, Zintl phases with the $CaAl_2Si_2$ structure type shown in Fig. 1a)[21,22] have attracted a great deal of attention as thermoelectrics[23]. Since their discovery[24,25], binary and ternary phases crystallizing in this structural pattern have been widely studied within the solid-state chemistry community with efforts focused primarily on determining the stability limits of the structure[26–34] and investigating the implications of the unusual anion coordination environment on the electronic structure[35,36], which ranges from metallic to insulating. In 2005,

Department of Chemical Engineering and Materials Science, Michigan State University, East Lansing, MI, USA.

† Electronic Supplementary Information (ESI) available: [details of any supplementary information available should be included here]. See DOI: 10.1039/b000000x/

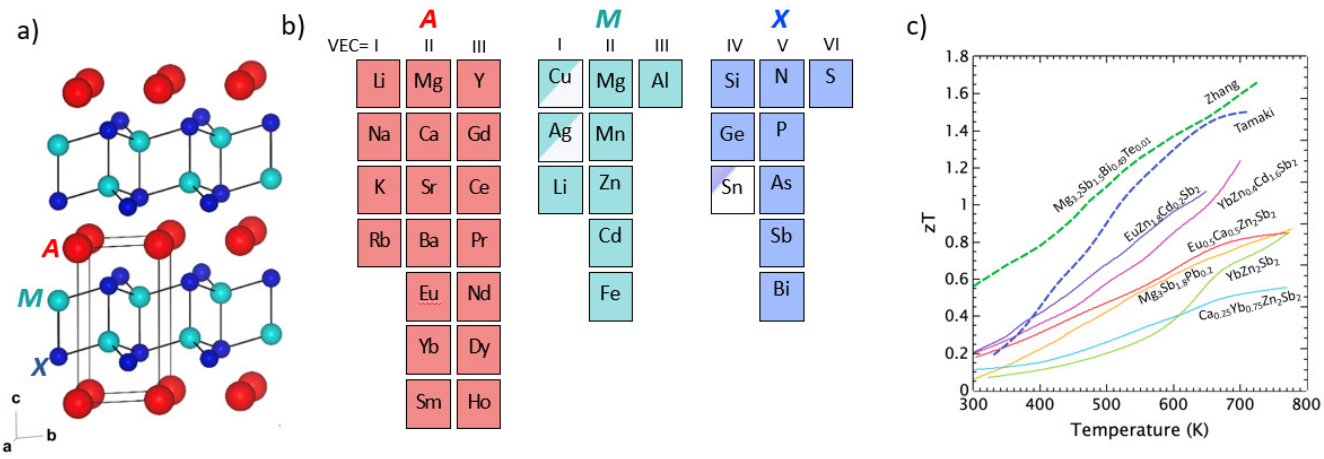


**Fig. 1** a) The $CaAl_2Si_2$ structure type is formed from 2-dimensional $Al_2Si_2$ anionic layers separated by a monolayer of 8-fold coordinated Ca. b) This structure type is formed by $AM_2X_2$ compounds with the following species $A$, $M$, and $X$, organized by nominal valence electron counts (see ESI Table 1 for a full list of compounds). c) The $zT$ of selected $n$-type (dashed curves) and $p$-type (solid curves) $AM_2X_2$ compounds [14–20].

Gascoin et al. reported promising thermoelectric properties in the $Ca_xYb_{1-x}Zn_2Sb_2$ solid solution [20], which spurred an initial series of studies on antimonides with the $CaAl_2Si_2$ structure type [16,37–40]. Although $CaAl_2Si_2$ itself is metallic, most of the antimonide and bismuthide compounds in this structure type are narrow band gap semiconductors, and exceptional thermoelectric performance has now been demonstrated in many members of this structural family (Fig. 1c)).

Compared with other classes of Zintl phases, $CaAl_2Si_2$-type compounds have several important advantages, the foremost being the unprecedented tunability of the $CaAl_2Si_2$ structure type. This is illustrated by Fig. 1b), which lists all elements that are known to substitute fully (or partially in a few instances) on the $A$, $M$, and $X$ site in the structure. In total, more than one hundred compounds have been reported to crystallize in this structure type. Those that have been investigated as thermoelectric materials (primary antimonides and bismuthides) have been found to possess light effective mass, leading to very high electronic mobility compared with other Zintl thermoelectrics [40]. However, they also have relatively high lattice thermal conductivity and, in many cases, low melting temperatures compared to other well-known Zintl thermoelectrics such as $Ca_5Al_2Sb_6$ [41] and $Yb_{14}MnSb_{11}$ [13].

The tunability of compounds with the $CaAl_2Si_2$ structure type provides many different routes for controlling the transport properties. The last decade of research has produced a large body of work aimed at optimizing the thermoelectric performance via band engineering [15,17,23,42] control of defect concentrations, [43,44], aliovalent doping [45], and point defect phonon scattering [9,16,20,38,46–49]. During this time, huge strides have been made in the field's understanding of the electronic structure and transport properties of these materials. Most recently, interest in these materials has redoubled, as Tamaki et al. reported the first instance of $n$-type $Mg_3Sb_2$ - a binary variant of $CaAl_2Si_2$ structure type - with higher efficiency than any of the previously reported $p$-type analogues (see Fig. 1c)) [14]. Our aim in the present review is to summarize past and current research on the structure, bonding, and thermoelectric properties of layered $AM_2X_2$ intermetallic compounds. We highlight recent progress made by both the solid-state chemistry and thermoelectric communities, and we look for general trends that can be applied to other Zintl phases or more broadly to other classes of thermoelectric materials. Finally, we discuss several aspects of the behavior of $AM_2X_2$ compounds that are critical to their performance but remain poorly understood, and propose opportunities for further investigation.

## 2 Structure and stability of $AM_2X_2$ compounds

The structure of $CaAl_2Si_2$ consists of two-dimensional $[Al_2Si_2]^{2-}$ slabs formed by $AlSi_4$ tetrahedra that share three of their edges with neighboring tetrahedra. Overall charge balance is provided by trigonal monolayers of $Ca^{2+}$ situated in the $a$-$b$ plane, which are coordinated by six Si (nearest neighbors) and six Al (next-nearest neighbors). The structure and cation coordination is illustrated in Fig. 3a). This structure can also be viewed as Si atoms in a hexagonal closed packed arrangement with half of the interstitial tetrahedral sites occupied by Al and half of the interstitial octahedral sites filled with Ca cations. An excellent description of the structure and bonding in $CaAl_2Si_2$ can be found in Ref. [35]. Here, we are primarily concerned with the stability limits of this structure type; in other words, what knobs can we turn as we attempt to control the thermoelectric properties, and how far can we turn them?

### 2.1 Electron counting and the Zintl-Klemm formalism

Zintl phases, named after the German scientist Eduard Zintl, are intermetallic compounds that consist of covalently-bonded polyanions surrounded by cations which provide overall charge balance, assuming complete charge transfer from the cation to the anions [6,57]. A simple electron counting scheme can be used to rationalize the anionic structures of Zintl phases. This rule holds that the number of covalent bonds per anion is equal to $8\text{-}VEC_{anion}$, where $VEC_{anion}$ is the number of valence electrons available per formula unit divided by the number of anions [6].

**Table 1** Compounds with the $CaAl_2Si_2$ structure can be classified according to the valence electron contribution from each site.[50–56] . Compounds with a total valence electron count of *VEC* = 16 are considered to be valence precise.

| Valence electron contribution | | | | Example | Ref. |
|---|---|---|---|---|---|
| $A$ | $(M)_2$ | $(X)_2$ | Total | | |
| II | $(II)_2$ | $(V)_2$ | 16 | $CaMg_2Sb_2$ | [50] |
| II | $(III)_2$ | $(IV)_2$ | 16 | $CaAl_2Si_2$ | [51] |
| III | (II)(III) | $(IV)_2$ | 16 | $GdZnAlGe_2$ | [52] |
| III | $(I)_3$* | $(V)_2$ | 16 | $GdLi_3Bi_2$ * Filled variant | [53] |
| III | (I)(II) | $(V)_2$ | 16 | $GdAgZnAs_2$ | [54] |
| I | $(II)_{1.5}(IV)_{0.5}$ | $(V)_2$ | 16 | $NaZn_{1.5}Si_{0.5}As_2$ | [55] |
| I | $(II)_{1.6}$* | $(VI)_2$ | 16.2 | $NaFe_{1.6}S_2$ * $M$ vacancies | [56] |
| III | $(III)_2$ | $(IV)_2$ | 17 | $GdAl_2Si_2$ | [52] |

Depending on the polarity[58,59] of the $M$-$X$ bond in $AM_2X_2$ Zintl phases, the metal, $M$ can be considered to be an anion, forming 2-center 2-electron bonds with $X$, or a cation with a closed outer valence shell. In $CaAl_2Si_2$, for example, the Al can be considered to be an anion. The total number of valence electrons per formula unit is 16, so we find that $VEC_{anion} = 16 / 4 = 4$. Since 8-$VEC_{anion} = 4$, we expect both Al and Si to be four-bonded (consistent with the observed structure). Thus, for this compound, the electronic charge can be simplified to $[Ca^{2+}][(4b)Al^{-}]_2[(4b)Si^{0}]_2$[35]. As the electronegativity difference becomes greater, this description is no longer accurate. In the extreme case of the nitrides (e.g., $CaMg_2N_2$), we would clearly not expect equal charge distribution between Mg and N ions. Y. Grin et al. showed that already in the case of $YbCd_2Sb_2$, the Cd is better described as a cation with a closed shell configuration: $[Yb^{2+}][Cd^{2+}]_2[Sb^{3-}]_2$[16]. In this case, the $VEC_{anion} = 16/2 = 8$, and the number of covalent bonds is formally zero. Regardless of the nature of the $M$-$X$ bond, however, 16 valence electrons per formula unit ($VEC = 16$) are necessary to satisfy the valence requirements of compounds in this structure type.

### 2.2 The multiple paths to 16 valence electrons

Nearly all of the $AM_2X_2$ compounds reported with the $CaAl_2Si_2$ structure (see EST Table 1 and 2) have 16 valence electrons per unit cell. The only exception to this rule are compounds lacking a band gap, such as the silicides and germanides, in which the energetic penalty for filling anti-bonding states is minimal. Thus, the metallic $RE Al_2Si_2$ and $RE Al_2Ge_2$ series ($RE$= lanthanide rare earth metal) have $VEC = 17$[60]. The remaining compounds in the $CaAl_2Si_2$ structure have $VEC = 16$, and can be classified according to the nominal valence electron contribution from $A$, $M$, and $X$, as we have shown in Table 1.

To date, the thermoelectric community has focused almost entirely on compounds containing divalent cations, e.g., alkaline earth metals (Mg, Ca, Sr, Ba) and rare earth metals (Yb, Eu, and Sm[61]). If $A$ is divalent, the valence electron count for the $M_2X_2$ substructure must be 14, which can be achieved with a divalent metal plus a group $V$ anion ($M$ = Mg, Mn, Zn, Cd, and $X$ = N, P, As, Sb, Bi). All reported thermoelectric studies concern compounds in this group[23]. Note that when $A = M$ = Mg, we obtain the binary variant of this structure type, which was discovered by Zintl in 1933[25]. Alternatively, divalent cations together with a trivalent metal and a group IV anion ($M$=Al and $X$=Si or Ge) are valence precise Zintl phases, but as mentioned above, these do not have band gaps[62], and thus are not of interest for thermoelectric applications.

Less attention has been given to the thermoelectric properties of compounds containing monovalent and trivalent cations. $VEC = 16$ is made possible in such compounds by adjusting the charge on the anionic slabs in order to achieve overall charge balance. For example, valence precise compounds with trivalent cations (e.g., lanthanides) can be formed by subtracting electrons from the anionic layers to compensate for the extra charge from the cation, e.g. $Gd^{3+}[Zn^{2+}Al^{3+}][Ge^{4-}]_2$[52] or the $RE^{3+}[Cu^{1+}Zn^{2+}][As^{3-}]_2$ series, where $RE$ = Ce, Dy, Nd, Sm, Tb[54]. The same game can be played in reverse with monovalent cations. This was demonstrated by A. Mar et al. in a series of compounds with alkali metal cations (Na, K, and Rb) in which mixed occupancy on the $M$ site was used to compensate for the missing electron on the cation site (e.g., $Na^{1+}[Zn^{2+}]_{1.5}[Si^{4+}]_{0.5}[As^{3-}]_2)$[63]. Another example, and the only known chalcogenide with the $CaAl_2Si_2$ structure, is the sulfide with nominal synthetic composition of $NaFe_{1.6}S_2$[56]. This compound contains a large fraction of vacancies on the $Fe^{2+}$ site, leading to a nominal total valence electron count of $VEC = 16.2$. However, the semiconducting behavior observed in these samples suggests that their true composition is closer to $VEC \sim 16$.

Yet another path to a $VEC = 16$ is provided by a series of compounds that form what is best described as a "filled" variant of the $CaAl_2Si_2$ structure type. In this structure, the octahedral interstitial site at (0,0,1/2) is fully occupied by Li, as illustrated in Fig. 2. These compounds have stoichiometry $ALi_3Pn_2$ where $A$ is a trivalent cation such as Ce-Nd, Sm, Gd-Ho and $Pn$ = a pnictogen species. Additional rare-earth containing compounds with $M$ = Cu and Li interstitials were recently reported by E. Jang et al.[53,65,66]. It is notable that the Li interstitial site in these examples is also where interstitial Mg is thought to reside in the $n$-type $Mg_3Sb_2$-based compounds, which will be discussed later.

Taken as a whole, the groups of compounds listed in Table 1 show that, so long as the $VEC = 16$ rule is satisfied, there is a

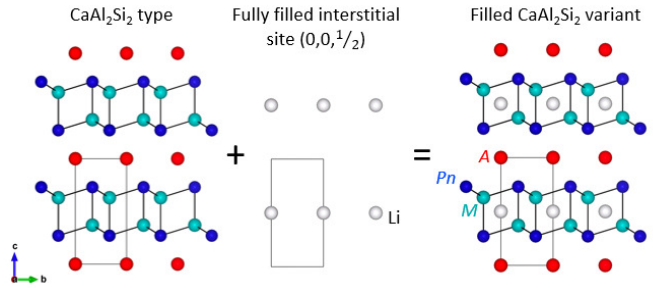


**Fig. 2** The filled variant of the $CaAl_2Si_2$ structure type (space group $P\bar{3}m1$, Pearson symbol $hP6$) is formed by adding Li atoms in the octahedral site at (0,0,1/2). The filled variant has stoichiometry $A(M,Li)_3Pn_2$, where $A$ = a trivalent cation, $M$ = Cu or Li, and $Pn$ = a pnictogen species[53,64–66].

great deal of flexibility in how the requirement is met. The cation valence ranges from 1-3, while the corresponding valence electron count on the anionic slab can vary between 13-17, achieved via mixed occupancy, vacancies, or interstitials. This suggests that there are many more options for tuning the composition of $AM_2X_2$ compounds than has thus far been exploited by the thermoelectric community. Similar substitutions to those used for skutterudites (e.g. $CoSb_3 \rightarrow CoGe_{1.5}Te_{1.5}$[86]) and diamond like semiconductors (e.g., $CuGaTe_4$[87]), can likely be used here. For example, one might consider partly replacing divalent Zn by a monovalent and a trivalent metal, or replacement of Bi by a group IV and V species, thus providing new routes to reducing thermal conductivity or controlling the carrier concentration.

### 2.3 Stability of $CaAl_2Si_2$ relative to other structure types

The $CaAl_2Si_2$ structure type is one of several structures that can be formed by intermetallic phases with the $AM_2X_2$ stoichiometry. In the context of this review, we will constrain ourselves to discussing only structures that are valence precise when $VEC$ = 16 electrons per formula unit. Within these constraints, there are two important structural patterns that compete thermodynamically with the $CaAl_2Si_2$ pattern: these are the orthorhombic $BaCu_2S_2$ structure ($Pnma$), and the tetragonal $ThCr_2Si_2$ structure family ($I4/mmm$)[88].

Compounds with the orthorhombic $BaCu_2S_2$ structure are typically semiconducting, and have shown promise as thermoelectrics with $zT$ as high as 0.67 at 900 K for $Ba_{1-x}K_xZn_2As_2$[16,89] The structure, illustrated in Fig. 3b), contains a cage-like 3D network of $M$ and $X$ atoms with two local tetrahedral environments, regular and distorted, for the $M$ atoms. The cations are coordinated by seven $X$ atoms and nine $M$ atoms arranged in a capped trigonal prismatic configuration[90,91]. Only a handful of compounds crystallize in this structure type (tabulated in the ESI Table 4), and very few reports of their thermoelectric transport properties have been published[16,89]. However, as these compounds are valence-precise semiconductors with complex, clathrate-like unit cells, we would expect them to exhibit excellent thermoelectric properties with optimized carrier concentration.

In contrast, the tetragonal $ThCr_2Si_2$ structure type (Pearson symbol $tI10$), a ternary variant of the $BaAl_4$ pattern, is one of the most ubiquitous intermetallic structure types known[92,93]. Compounds with this structure or a variant thereof have been studied extensively due to their remarkable magnetic properties and superconductivity[94,95]. The $ThCr_2Si_2$ structure consists of $M_2X_2$ layers made up of $MX_4$ tetrahedra which share four of their six edges. The layers are separated by cations occupying the square prismatic interstitial sites, in 8-fold coordination with respect to $X$ (see Fig. 3c). An extraordinary feature of this structure type, is that the distance between the layers varies greatly depending on whether or not covalent bonds form between the opposing apical anions[93]. This flexibility in the bonding means that the valence electron count can range from 12-16, and the interlayer bonding adjusts accordingly. However, even when no interlayer bonds are present, there is significant overlap of the anion $p_z$ orbitals that bridge between the anionic layers. The electronic states associated with the $p_z$ orbitals tend to reduce the band gap, leading to semi-metallic or metallic behavior. For example, Xiao et al. calculated the band gaps of $AZn_2As_2$ ($A$ = Ba, Sr, and Ca) with the tetragonal $ThCr_2Si_2$ and trigonal $CaAl_2Si_2$ structures using hybrid functionals, and found that the gap in the trigonal structure were consistently 0.6 eV larger[96]. Compounds in the $ThCr_2Si_2$ structure type are thus almost exclusively metallic, and have not been their thermoelectric transport properties have not been studied.

Among $AM_2X_2$ compounds with $VEC$ = 16, the majority form the trigonal $CaAl_2Si_2$ structure type, while compounds with $VEC$ < 16 overwhelmingly prefer the tetragonal $ThCr_2Si_2$ structure type[88]. There are a number of compounds, however, that form either the orthorhombic or tetragonal structure types even though they have $VEC$ = 16. Several authors have noted that the size of the cation plays an important role in determining which structure is adopted[30,63]. Compounds with smaller cations tend to favor the $CaAl_2Si_2$-type structure, in which the cation is coordinated by six $X$ atoms, while the $BaCu_2S_2$ or $ThCr_2Si_2$-types structure are preferred for larger cations due to the 7-fold and 8-fold coordination, respectively. This is illustrated by the phase map in Fig. 3d), which shows the electronegativity difference between $M$ and $X$ versus the weighted function of the atomic radii, $f = r_A/(r_M + 0.2r_X)$, where $r_A$, $r_M$,and $r_X$ are the Slater atomic radii for $A$, $M$, and $X$[30,97]. Here, we include the empirical factor of 0.2 used by Klüfers et al.[30] to better delineate the stability range of the $CaAl_2Si_2$ structure type. In contrast to the atomic radii, the electronegativity does not appear to play an important role in determining the stability limits of the $CaAl_2Si_2$ structure type.

Applied temperature and/or pressure can lead to transitions between these three structure types[98–100]. In $SrAl_2Si_2$, pressure has been used to induce the transition from the $CaAl_2Si_2$-type into the $ThCr_2Si_2$-type pattern, while in $BaAl_2Si_2$, pressure leads to a transition from the $BaCu_2S_2$ into the $ThCr_2Si_2$-type pattern. These transitions are both consistent with the empirical rule that high pressure stabilizes phases with higher coordination numbers[101]. It is likely that additional compounds with the trigonal structure type will transform under pressure to either the $ThCr_2Si_2$ or $BaCu_2S_2$ structure types as well, providing a potential route to further study the relation between structure and properties in this class of materials.

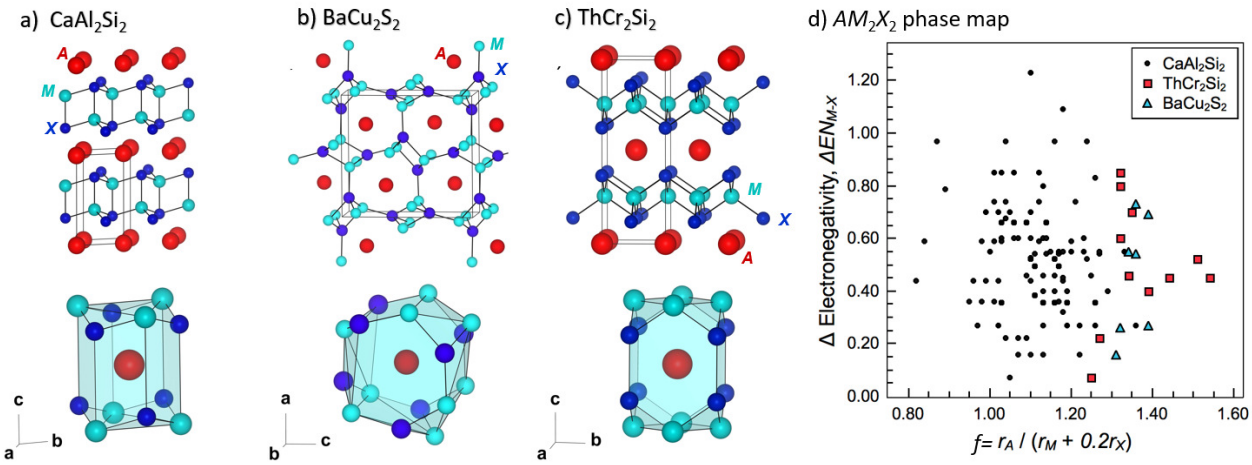


**Fig. 3** Structure types formed by $AM_2X_2$ compounds with $VEC$ =16 include a) the trigonal $CaAl_2Si_2$ structure type ($P\bar{3}m1$), b) the orthorhombic $BaCu_2S_2$ structure type ($Pnma$), and c) the tetragonal $ThCr_2Si_2$ structure type ($I4/mmm$). d) The stability range of each structure can be delineated as a function of the atomic radii, $f = r_A/(r_M + 0.2r_X)$, while the polarity of the $M$-$X$ bond is clearly not a deciding factor. A complete list of the compounds included in this phase map are outlined in ESI Tables 1-3 [22,25–34,50,52,60,67–85].

## 3 Synthesis and crystal growth approaches

The majority of experimental thermoelectric transport data for $AM_2X_2$ compounds were measured on polycrystalline samples. Unless otherwise noted, all of the thermoelectric transport data discussed in this review are from polycrystalline samples. Single crystal growth of $AM_2X_2$ compounds has primarily been used to obtain small crystals necessary for structure determination. In a few cases, large single crystals suitable for transport measurements have been grown. Below, we give a brief overview of some of the routes used to synthesize $AM_2X_2$ compounds.

Small single crystals have been grown primarily via flux or self-flux for a large number of compounds including $RELi_3Sb_2$ ($RE$ = Ce-Nd, Sm,and Gd) [66] grown in Pb flux, $AAl_2Si_2$ ($A$ = Eu, Yb) in an Al flux [102], and $SmMg_2Sb_2$ and $SmMg_2Bi_2$ grown in a Mg-Sb and Mg-Bi flux respectively [61]. $AMg_2Bi_2$ [77] and $AZn_2Sb_2$ [103] ($A$ = Ca, Eu, Yb) crystals were grown in Mg-Bi and ZnSb flux, respectively, and in this case, transport measurements were made in the in-plane direction. Small crystals (< 0.3 mm) can also been obtained from stoichiometric melting of compounds and subsequent annealing in the presence of an additive such as iodine to promote the growth of crystals as in the case of $RECuZnAs_2$, $REAgZnP_2$ and $REAgZnAs_2$ ($RE$ = Y, La-Nd, Sm, Gd-Lu) [54]. There are very limited examples of large single crystals grown for compounds with the $CaAl_2Si_2$ structure type. These include large (10 mm × 60 mm) $CaAl_2Si_2$ crystals grown from the melt using the floating zone technique [104], and $Mg_3Sb_{2-x}Bi_x$ crystals (10 mm × 25 mm) [105,106] grown using the Bridgman technique.

Most of the methods used to synthesize consolidated polycrystalline samples for transport measurements fall into one of two categories: The first consists of a solid-state reaction approach in which an annealing or melting step is followed by a pulverization and subsequent consolidation via spark plasma sintering (SPS) or hot pressing. This has been applied to many of the antimonides [38,107], bismuthides [108], and even phosphides [46]. The second route involves high-energy ball milling of stoichiometric amounts of elements or precursors, followed directly by a high temperature sintering step in an SPS or hot press. This approach has been used for many recent results [14,17,18,43,109]. In at least one example, arc-melting was also incorporated into the ball-milling and consolidating process such as in Zhang et al.'s synthesis of $Mg_3Sb_{1.5}Bi_{0.5}$ [110]. In some instances, multiple routes have been used to synthesize the same compound, as in the case of $EuZn_2Sb_2$ and $YbZn_2Sb_2$ [40,43,107,109].

Defect concentrations in $AM_2X_2$ compounds are extremely sensitive to the synthesis conditions, as discussed in depth below. In particular, processing routes with long annealing steps or very high temperatures (i.e., arc-melting), can lead to losses of high vapor pressure or reactive elements and thus shifts the composition away from the intended stoichiometry [23]. Crystal growth using a self-flux (i.e., $AZn_2Sb_2$ grown in ZnSb flux) will shift the chemical potential, thus influencing the intrinsic defect formation enthalpies [14,111]. Careful consideration of the synthesis conditions and their impact on defect formation should therefore accompany any attempts at controlling carrier concentration. Further, the carrier mobility is highly dependent on the grain size and grain boundary characteristics, which are also dependent on the processing route. This leads to large variation in the performance of samples at room temperature, but does not greatly impact the high temperature transport [112].

## 4 Electronic structure

### 4.1 Band gap and electronegativity

The features of the electronic band structure that determine a material's potential maximum figure of merit include the band gap ($E_g$), the number of degenerate bands near the Fermi level ($N_v$) and the band effective mass ($m_b^*$). The size of the band gap is one of the most critical properties of a material, even though it is not explicitly included in expressions for the thermoelectric quality factor. Here, as with many aspects of thermoelectric material design, a balance must be struck; a larger band gap reduces the

contribution from minority carriers and increases the temperature of the peak $zT$, but a smaller gap may make it easier to shift the Fermi level to optimize $zT$ [113]. The majority of excellent thermoelectric materials are thus narrow band gap semiconductors with $E_g$ = 0.2 - 1.0 eV.

Given the enormous chemical diversity of $AM_2X_2$ compounds, it is not surprising that their electronic structure varies from metallic ($E_g$ = 0) to insulating ($E_g$ > 3 eV), depending on the composition. The width of the band gap is strongly dependent on the anion, and in particular the electronegativity difference, $\Delta EN$, between $M$ and $X$. This can be as low as 0.3 in $CaAl_2Si_2$ and up to 1.7 in $CaMg_2N_2$. This relationship is illustrated by Fig. 4b), which shows the calculated band gaps for compounds with $M$ = Mg using data from the Materialsproject.org [114]. A recent study by Singh et al. also demonstrated this relationship, showing that the band gap is relatively insensitive to the cation, $A$, but increases with the electronegativity of the anion, $X$ [115].

The strong influence that the anion has on $E_g$ can be understood conceptually using the simplified molecular orbital diagram in Fig. 4a) [116,117], which shows the bonding $MX$ and anti-bonding $MX^*$ interactions. $E_g$ is a function of the difference in energy between the atomic $M$ and $X$ valence orbitals (2$A$), the bond energy (2$B$), and the width of the bands ($W_{CB}$ and $W_{VB}$). A larger $\Delta EN_{M-X}$ is expected to increase 2$A$, thus increasing $E_g$. The smaller anions (e.g., P or N) would also be expected to lead to smaller orbital overlap, in turn decreasing $W_{CB}$ and $W_{VB}$, and further increasing the size of the gap. Experimental band gaps, estimated using the Goldsmid-Sharp equation ($E_g = 2\alpha_{max}T_{max}$) also support the conclusions above. When the cation species is varied, the band gap remains nearly constant, e.g., $YbZn_2Sb_2$ (0.25 eV) and $CaZn_2Sb_2$ (0.27 eV) [19], or $CaMg_2Bi_2$ (0.2 eV), $EuMg_2Bi_2$ (0.2 eV), $YbMg_2Bi_2$ (0.3 eV) [103]. However, the band gap increases when the electronegativity of $X$ increases and $M$ remains unchanged, e.g., $Mg_3Bi_2$ (0.0 eV), $Mg_3Sb_2$ (0.46 eV) [111], $CaMg_2N_2$ (3.25 eV) [118].

It should be noted that the band gaps of most $AM_2X_2$ compounds are severely underestimated by density functional theory calculations using GGA functionals, meaning that any compound with $E_g$ > 0.3 eV may be predicted to be metallic. The predicted metallic behavior [62] in all $AM_2X_2$ compounds with $X$ = Si or Ge are most likely accurate, as the metallic behavior has been experimentally verified in some cases [104,119,120]. However, all $AZn_2Sb_2$ and $ACd_2Sb_2$ compounds ($A$ = Ca, Sr, Yb, Eu) are predicted to be metallic, but experimentally they exhibit semiconducting behavior [40,121]. Thus, many of the compounds with ideal $E_g$ for thermoelectric applications are predicted to be metals, which complicates first-principles modeling efforts and data mining via high-throughput calculations. For some purposes, corrections such as the modified Beck-Johnson functional [115,122–124] can be used to yield accurate band gaps. However, to obtain accurate total energies *and* band gap values, more expensive hybrid functionals are necessary.

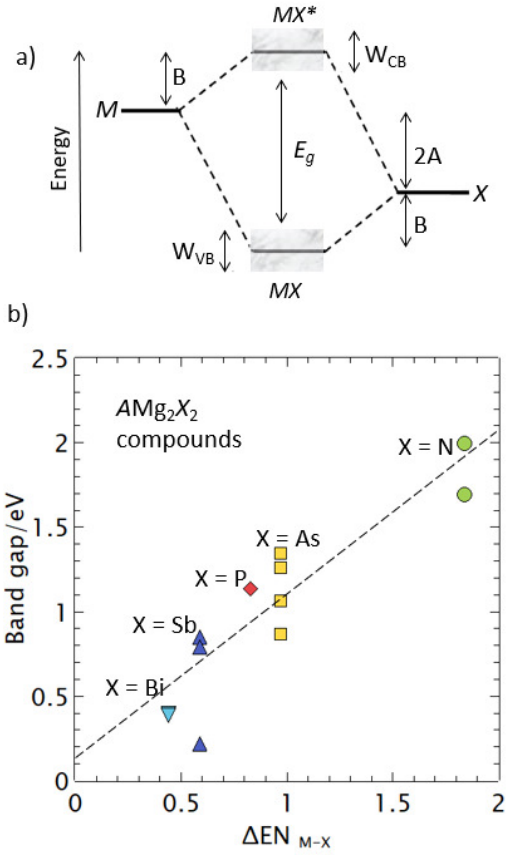


**Fig. 4** a) A simplified molecular orbital diagram shows the bonding and anti-bonding states from the polar covalent $M-X$ bonds with the energy between the atomic orbitals (2$A$), the bond energy (2$B$), and the width of the bands ($W_{CB}$ and $W_{VB}$). b) The calculated $E_g$ in $AMg_2X_2$ compounds increases as $X$ becomes lighter due to decreased orbital overlap and increased $\Delta EN_{M-X}$. Band gap values from MaterialsProject.org [114] and electronegativity using the Allred-Rochow scale.

### 4.2 Valence and conduction band characteristics

The electronic structures reported to date for semiconductors with the $CaAl_2Si_2$ structure type share several common features: the valence band maximum is dominated by the anion $p$-orbital states, while the conduction band minimum is comprised of a combination of cation $s$- or $d$-orbitas and $MX$ anti-bonding states [127]. The valence band maximum ($VBM$) is always centered at the Γ point, while the k-space position of the conduction band minimum ($CBM$) depends on composition. It often falls along a 6-fold symmetry axis, near the high symmetry points M and L. The band gap thus can be direct or indirect, depending on which of the pockets in the conduction band form the $CBM$. The calculated band structure and Fermi surfaces of $Mg_3Sb_2$ by Zhang et al. are shown in Fig. 5a). Here, the valence band is at Γ with $N_v$ = 1, and the conduction band minimum labeled $CB1$ between M* and L* has a degeneracy of six due to symmetry. The conduction band pockets at the K point (labeled $CB2$) and at the Γ point can play a role as well, as described below. [15,115,128].

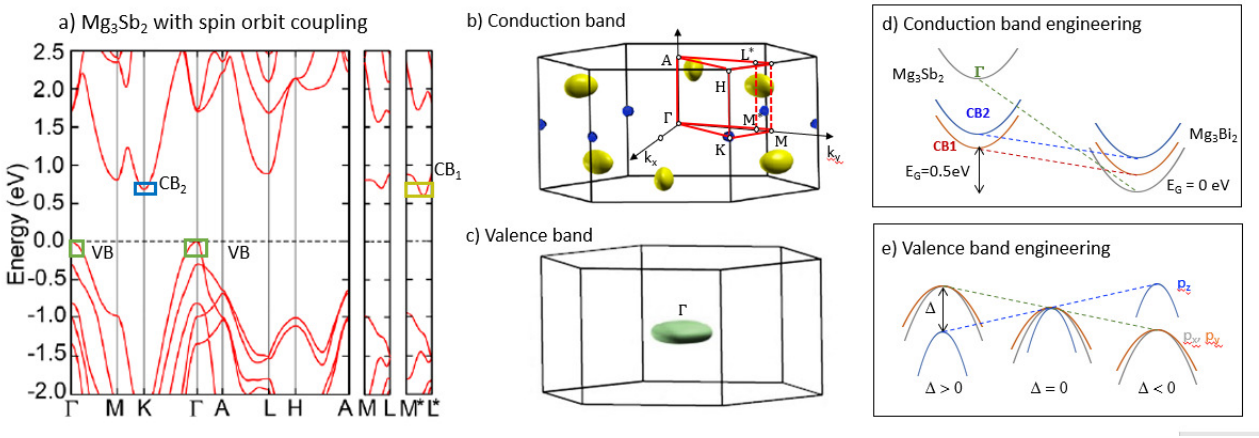


**Fig. 5** a) The electronic band structure and b-c) Fermi surface of the valence and conduction bands of $Mg_3Sb_2$ from Ref. [15] including spin orbit coupling. Figure reproduced with permission from Ref. [42]. Band engineering of the d) conduction band and e) valence band aim to converge multiple bands near the Fermi energy [125,126].

### 4.3 Band Engineering

Band engineering strategies have been proposed to increase the degeneracy of both the conduction and valence band edges in $AM_2X_2$ compounds. The degeneracy near the Fermi energy is an important factor for the thermoelectric performance of a material, as high $N_v$ increases the density of states effective mass ($m^*_{DOS}$), which can in turn increase the power factor [1,129]. High $N_v$ combined with light band effective mass, $m^*_b$, and minimal inter-valley scattering is the basis of success for most of the highest performing thermoelectric materials.

For $p$-type samples, $N_v$ is maximized when the three anion $p$-orbitals, $p_x$, $p_y$, and $p_z$, are converged [42]. For most of the $AM_2X_2$ compounds, the light out-of-plane $p_z$ band is usually separated from the heavier doubly-degenerate in-plane $p_{x,y}$ bands. One approach proposed to minimize this energy gap ($\Delta$) between $p$-orbital bands is to form solid solutions to adjust the $c/a$ ratio, which can minimize the crystal field splitting energy of orbitals (as shown in Fig. 5e)) [42]. However, it should be noted that reasonable and attractive as it seems, attempts to experimentally control the band convergence of the valence bands has not led to significantly improved $zT$ values. The maximum $N_v$=3 due at the high symmetry Γ point can be considered as a limiting factor in the $zT$ value of $p$-type $AM_2X_2$ compounds.

Compared with the valence band, the complex conduction band Fermi surface in $AM_2X_2$ compounds is more favorable for thermoelectric applications. The conduction band consists of valleys at Γ ($N_V$ = 1), between $M^*$ and $L^*$ ($N_v$ = 6), and at $K$ ($N_v$ = 2) [115,128]. Note that the degeneracy of the latter is because only a third of each of the six pockets shown in Fig. 5b) is inside the first Brillouin zone. The relative energies of each of these minima is highly sensitive to composition. Substituting heavier atoms on the anion site leads to a downward shift in the valley at the Γ point. This effect was demonstrated in the $Mg_3Sb_{2-x}Bi_x$ solid solution [44], as illustrated schematically in Fig. 5d). The CB1 and K band are very near to each other, but separated from the Γ band. Alloying with Bi reduces the energy of the Γ band, leading to convergence, and eventually to complete closing of the band gap. The band effective mass will also decrease due to the interaction between conduction band edge and valence band edge, leading to an increase in mobility. A proper doping level of less than 25% is crucial to enhance mobility without the negative impact of the bipolar effect. The same effect can be observed in the series $AMg_2Pn_2$ where $A$=Ca, Sr, Ba, and $Pn$=As, Sb, and Bi [115]. The cation has little effect on the relative energies, but changing the anion leads to convergence of the conduction band pockets, lighter bands, and a decrease in $E_g$.

## 5 Tuning the carrier concentration

Although the presence of a band gap is perhaps the most critical requirement for high $zT$, the ability to tune and optimize the carrier concentration is a close second. For $AM_2X_2$ compounds, the ideal carrier concentration is typically in the range of $2.5 \times 10^{19}$ to $6.5 \times 10^{19}$ carriers/$cm^3$. In most thermoelectric material systems, heavily-doped, extrinsic behavior is achieved by doping with an aliovalent atom (e.g., Na in PbTe). In this regard, the study of $AM_2X_2$ compounds has been unique, in that carrier concentration optimization is most often carried out by either exploiting or suppressing the high defect concentrations native to these materials, via either isovalent substitutions or by controlling the synthesis conditions.

### 5.1 Cation vacancies and $p$-type behavior

It is common for nominally valence-precise $AM_2X_2$ compounds with $E_g > 0.2$ eV to show extrinsic $p$-type behavior with carrier concentrations of up to $1.5 \times 10^{20}$ holes/$cm^3$ [40]. This persistent $p$-type behavior arises due to the low formation enthalpy, $\Delta H_D$ of cation vacancies, $V_A$, which act as acceptor defects [43,124]. Fig. 6a) shows the dependence of $\Delta H_D$ on the Fermi level for $A$ site vacancies in $AZn_2Sb_2$ compounds ($A$ = Ca, Sr, Eu, Yb). As the Fermi energy is shifted towards the conduction band edge, the energy required to form $A$ site vacancies decreases, becoming negative within the band gap. Thus, any attempt to raise the Fermi level will be compensated by spontaneous formation of acceptor type defects. The cation vacancy formation enthalpy is sufficiently low

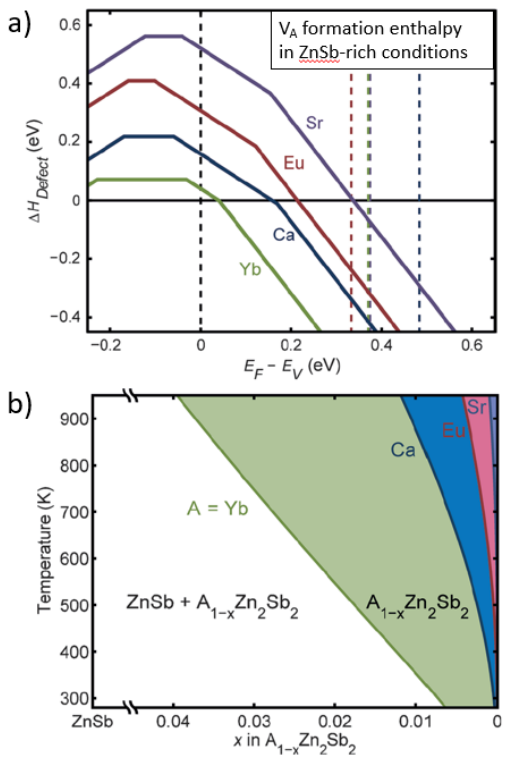


**Fig. 6** a) The defect formation energy, $\Delta H_D$, for cation vacancies in $AZn_2Sb_2$ compounds ($A$ = Ca, Sr, Eu, Yb) in equilibrium with ZnSb decreases with increasing cation electronegativity. The dashed lines denote the valence and conduction band edges for each compound. Figure reproduced with permission from Ref. [124]. b) The predicted pseudo-binary phase diagram shows the overlaid single-phase region for each $AZn_2Sb_2$ compound. Wider single phase regions corresponds to higher vacancy concentrations. Figure taken from Pomrehn et al. [124].

to lead to an appreciable phase width at high temperatures. In $Yb_xZn_2Sb_2$, for example, $x$ as low as 0.98 is predicted to be stable at 800 K (Fig. 6b)), corresponding to a $p$-type carrier concentration of $1.4 \times 10^{20}$ holes/cm$^3$. Varying the cation concentration, $x$, of $AM_2X_2$ samples within the single-phase region can be used to directly control and optimize the $p$-type carrier concentration, as shown in the case of $Yb_xZn_2Sb_2$ [43].

In addition, the defect energy of cation site vacancies is dependent on the electronegativity of the cation [124]. The relationship between $\Delta H_D$ and electronegativity is related to the relative energy cost of transferring electrons from the cation to the anions, which in turn influences bond strength and vacancy formation energies. High electronegativity cations such as Yb, tend to exhibit the lowest $\Delta H_D$ for cation vacancies, and thus the highest $p$-type carrier concentrations. The consequence of this, is that alloying on the $A$-site with elements of different electronegativity makes it possible to tune the carrier concentration, without the need for traditional aliovalent dopants. This effect was exploited in a number of optimization studies for $p$-type $AM_2X_2$ compounds, in which alloying led to samples with reduced $\kappa$ and $n_H$ shifted towards the optimal value. For example, the range of the carrier concentrations of $AZn_2Sb_2$ are from $1.5 \times 10^{19}$ carriers/$cm^3$ for $SrZn_2Sb_2$ and $1.5 \times 10^{20}$ carriers/$cm^3$ for $YbZn_2Sb_2$ with increasing electronegativity difference between the cation and polyanion.

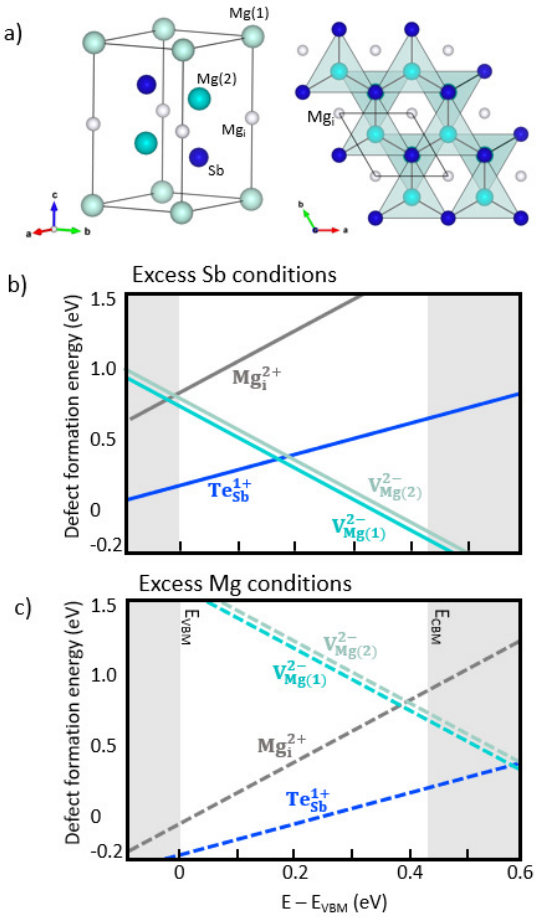


**Fig. 7** a) The crystal structure of $Mg_3Sb_2$ showing the possible Mg vacancy and interstitial sites. b) Defect formation energy in Sb excess conditions favors the formation of Mg vacancies, which act as "killer" defects when $n$-type doping is attempted. c) The defect formation energy in Mg excess conditions favor formation of Mg interstitials, which act as electron donors. Figure reproduced with permission Ref. [111].

### 5.2 $n$-type behavior in $Mg_3Sb_2$-based compounds

The ready formation of cation vacancies pins the Fermi energy below the conduction band edge, explaining why $n$-type doping has thus far been hard to achieve in $AM_2X_2$ compounds. For this reason, the possibility of $n$-type doping in compounds with the $CaAl_2Si_2$ type structure was overlooked until a recent study by Tamaki et al. in which $zT$ = 1.5 was reported in $n$-type $Mg_{3.2}Sb_{1.5}Bi_{0.49}Te_{0.01}$ synthesized with excess Mg [14]. Comparable $zT$ values have since been reported by several other authors for similar compositions [15,44,128] This is several times higher than that of the previous $p$-type $Mg_3Sb_2$ (Ag, Na or Pb doped) [130–132].

$Mg_3Sb_2$ is intrinsically $p$-type [133] because, as in the $AZn_2Sb_2$ compounds discussed above, cation site vacancies are one of the most stable types of defects in this system [14]. As shown in Fig. 7b) and c), the defect energies depend strongly on the synthesis conditions. If $Mg_3Sb_2$ is in equilibrium with Sb (Mg-deficient conditions), the formation enthalpy for Mg vacancies is low, pin-

ning the Fermi energy well below the conduction band edge, and precluding *n*-type behavior. If, in contrast, $Mg_3Sb_2$ is in equilibrium with Mg (excess Mg conditions), the energy of Mg(1) and Mg(2) vacancies increases, while the energy of forming Mg *interstitials* ($Mg_i$), decreases drastically. The Mg interstitial site is at (0,0,1/2), the same as the well-documented Li interstitial site in the filled-variant of the $CaAl_2Si_2$ structure discussed earlier[14,111]. Ohno et al. were able to systematically demonstrate the importance of the synthesis conditions with a series of samples in which the Te doping was kept constant, while the Mg content was varied. Mg-deficient samples were *p*-type while Mg-excess samples were *n*-type. Samples with nominal compositions of $Mg_3Sb_{1.99}Te_{0.01}$ exhibited n-type behavior however, suggesting that as long as sufficient care is taken in synthesis to avoid Mg loss, excess Mg is not strictly necessary to obtain the *n*-type samples.

There are now opportunities to apply similar strategies to other $AM_2X_2$ compounds. Thus far, attempts to eliminate cation vacancies by simply adding excess Yb and Eu in $(Yb,Eu)_{1+x}Zn_2Sb_2$ samples during synthesis were unsuccessful in that they led to reduced hole concentrations, but not to *n*-type behavior[19,109]. The defect calculations shown in Fig. 7b) and c) point towards the need for a combined approach using both excess cations to shift the defect chemistry to favor *n*-type doping, combined with an aliovalent substitution of a suitable *n*-type dopant, such as Se or Te on the Sb site.

## 6 Transport analysis using an effective mass model

A simple yet powerful model for thermoelectric transport is the effective mass model, or single parabolic band (SPB) model[134]. We employ it here to assess the variability in the experimental density of states effective mass, $m^*_{DOS}$ and the carrier relaxation time of $AM_2X_2$ samples reported in the literature. Shown in Fig. 8a) are the room temperature Seebeck coefficients, $\alpha$, and Hall carrier concentration, $n_H$, of both *n*- and *p*-type $AM_2X_2$ samples. The source data can be found in the ESI Table 5. Note that we do not distinguish between pure and alloyed samples in this case. The *p*-type samples, on average, can be modeled using $m^*_{DOS} = 0.6\ m_e$. The upper and lower limits are roughly 0.9 $m_e$ and 0.5 $m_e$, respectively. Assuming that the band effective mass remains fairly constant, the variation of $m^*_{DOS}$ by about a factor of two is in good agreement with $m^*_{DOS} = N_v^{\frac{2}{3}} m^*_b$, where $N_v$ varies from 1 to 3. We note that much of the data included in this plot is for antimonides, and it is therefore not very surprising that the band effective mass shows little fluctuation.

The $m^*_{DOS}$ of *n*-type $Mg_3Sb_{2-x}Bi_x$ samples is approximately 1.2 $m_e$, or twice that of the average *p*-type sample. The high density of states effective mass arises from higher band degeneracy rather than from higher band mass; in $Mg_3Sb_2$, the calculated conduction band effective mass of 0.3 $m_e$ is actually slightly lower than the value of 0.36 $m_e$ for the valence band[15]. When comparing the difference in $m^*_{DOS}$ among *n*-type samples, the Bi-content is found to have a strong effect, decreasing the band effective mass due to the interaction between the valence and conduction band[44].

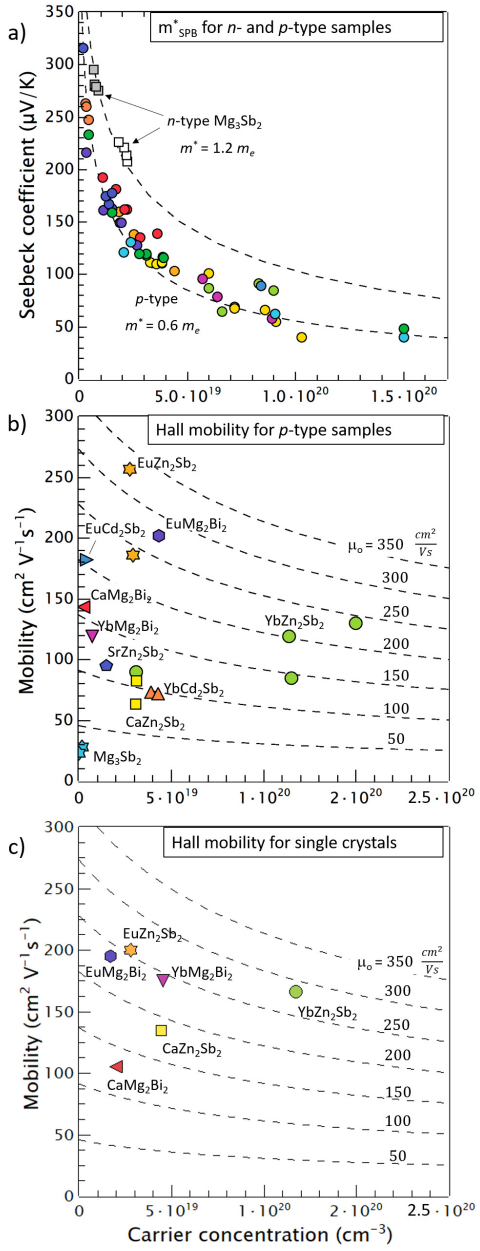


**Fig. 8** a) Experimental $\alpha$ and $n_H$ at room temperature. The Pisarenko curves were calculated assuming an effective mass of 0.6 $m_e$ and 1.2 $m_e$ for *n*-type and *p*-type samples, respectively. Each color corresponds to a different reference, listed in the ESI Tables 6 and 7. b) Experimental $\mu_H$ values for polycrystalline *p*-type non-alloyed samples, and c) for single crystalline samples (in-plane measurements)[77,135]. The dashed curves the dependence of mobility on $n$ within an SPB model assuming acoustic phonon scattering. Source data listed in the ESI Table 5.[15–17,20,37–39,43,47,128,130–132,134,136].

Fig. 8b) shows the room temperature Hall mobility, $\mu_H$, as a function of $n_H$ for *unalloyed* *p*-type samples. The dashed curves illustrate the expected carrier concentration dependence within an effective mass model with different values of the intrinsic mobility, $\mu_o$. This model assumes that acoustic phonon scattering is the only electron scattering mechanism, which is often not the case. The temperature dependence of the mobility and conductivity in

many cases indicates that other mechanisms, such as grain boundary[112] and ionized impurity scattering are important, especially at low and intermediate temperatures. We use room temperature data here, simply because few high-temperature Hall measurements are available in the literature. However, this makes it difficult to determine whether the large variation in mobility from one compound to another ($\mu_o$ varies from $\sim$ 30 - 300 cm$^2$/Vs) is inherent to the materials, or is due to processing or impurities.

To better answer this question, we can look to measurements of single crystals. May et al. measured the in-plane mobility in $A$Mg$_2$Bi$_2$ and $A$Zn$_2$Sb$_2$ ($A$ = Ca, Eu, Yb) crystals grown from Mg-Bi and Zn-Sb flux, respectively[77,103] (shown in Fig. 8c). At 300 K, the Hall mobility of these samples decreases with increasing temperature, indicating that an assumption of acoustic phonon scattering is reasonable. In comparing the single and polycrystalline results, the main conclusion that can be drawn is that the rare-earth containing samples ($A$ = Eu, Yb) have inherently higher mobility than alkaline earth containing samples. This is despite the fact that the ground-state valence band characteristics ($N_V$, $m_b^*$) do not vary significantly for different cations. Given the nearly constant effective mass, the difference in mobility can only be explained by the carrier relaxation time, $\tau$ ($\mu = \frac{e\tau}{m^*}$). The high mobility in compounds with rare-earth elements is still not well understood. May et al. noted that the Hall mobility correlates with the Debye temperatures of the compounds, suggesting that differences in the phonon dynamics play an important role[103].

## 7 Thermal transport

While the electronic structure and its compositional dependence has been the focus of several important studies, little is known regarding the lattice dynamics in compounds with the CaAl$_2$Si$_2$ structure. To date, only the phonon dispersions of CaMg$_2$Sb$_2$, Mg$_3$Sb$_2$, and Mg$_3$Bi$_2$ have been reported[44,115]. The calculated phonon dispersion and density of states (DOS) from Ref. [115] are shown in Fig. 10 for CaMg$_2$Sb$_2$. The 5-atom unit cell leads to a dispersion consisting of three acoustic and 12 optical modes. The partial DOS shows that the three acoustic modes and the lowest two optical modes are dominated by Sb, due to its higher atomic mass. The contribution from Ca defines the mid-frequency optical modes (4 to 5 THz) and the Mg contribution is constrained mainly to the highest frequency modes (5 to 8 THz). We note that there is no gap between acoustic and optical modes, and in fact the lowest-lying optical modes cross through the acoustic branches. This effect may lead to stronger than expected phonon-scattering. A systematic investigation the phonon dispersions and composition is still lacking, leaving many unanswered questions regarding the influence of density, mass contrast, possible lattice instabilities etc. in these phases.

For thermoelectric applications, Zintl phases are typically touted as having inherently low lattice thermal conductivity due to their structural complexity[2,23]. This relationship has been attributed in part to the large unit cells of some Zintl phases, which leads in turn to a large number of optical modes in the phonon dispersion, and thus to low average phonon group velocities[137]. The relatively small unit cell of the CaAl$_2$Si$_2$ structure type, however, means that the phonon dispersion is no more complex than materials such as PbTe, CoSb$_3$, etc.. Indeed, the lattice thermal conductivities, $\kappa_L$, of most $AM_2X_2$ compounds are not exceptionally low, at least as far as Zintl phases are concerned. Most high $zT$ $AM_2X_2$ compositions benefit from some degree of alloying to lower the lattice thermal conductivity via point defect scattering. This is in contrast to more complex Zintl phases, which do not benefit greatly from the effects of point defect scattering. To compare $\kappa_L$ across multiple compounds, we used the reported $\kappa_{total}$ and calculated $\kappa_e$ using the reported resistivity. The Lorenz number, $L$, was determined within the SPB model by using the reported Seebeck coefficients to estimate the reduced Fermi level (data listed ESI Table 5). The lattice thermal conductivities obtained in this way are plotted as the y-axis of Fig. 9. Only non-alloyed samples were considered here, as we wish to decouple intrinsic effects (anharmonicity, speed of sound) from alloying-induced point-defect scattering. Depending on the composition, $\kappa_L$ varies between 0.6 W/mK (CaCd$_2$Sb$_2$[49]) and 4.55 W/mK (CaMg$_2$Sb$_2$[138]).

Experimental values for the sound velocities and Grüneisen parameters are generally lacking for $AM_2X_2$ compounds. However, an estimate can be made for the mean speed of sound of each compound by employing the experimentally determined density and the bulk and shear elastic moduli obtained from MaterialsProject.org[139]. The predicted mean speed of sound is shown as the x-axis of Fig. 9. In polycrystalline samples, in the absence of strong boundary scattering or point defect scattering, lattice thermal conductivity is expected to be a strong function of the speed of sound. However, as shown in Fig. 9, the trend is not obvious. This highlights the significant impact of other factors that are contributing to the lattice thermal conductivity, such as the Grüneisen parameter, and additional scattering sources that depend on sample quality. In particular, it is surprising to see that Mg$_3$Sb$_2$ (Na and Ag doped $p$-type samples), which has stiffer bonds and lower density than most other $AM_2X_2$ compounds, exhibits lower $\kappa_L$. On the one hand, it is possible that the Mg$_3$Sb$_2$ samples simply have a greater degree of boundary scattering. However, the consistency of the results from different groups points towards intrinsically low $\kappa_L$ stemming from increased anharmonicity and phonon-phonon scattering.

## 8 Strategies for optimizing *zT*

The dimensionless figure of merit $zT$ of selected $AM_2X_2$ compounds as a function of temperature is shown in Fig. 1c). Optimizing the figure of merit in $n$-type and $p$-type $AM_2X_2$ compounds has been achieved via four basic routes: 1) decreasing the lattice thermal conductivity via point defect scattering, 2) increasing the electronic mobility, 3) varying the composition to achieve convergence of multiple bands and, most importantly, 4) tuning the carrier concentration. The latter two methods were described in detail above. Below, we discuss methods to reduce $\kappa_L$ and improve mobility. Ideally, all of these approaches must be used together to fully optimize performance. This is challenging in practice, as the carrier concentration is very sensitive to changes in composition, even when isoelectronic substitutions are used.

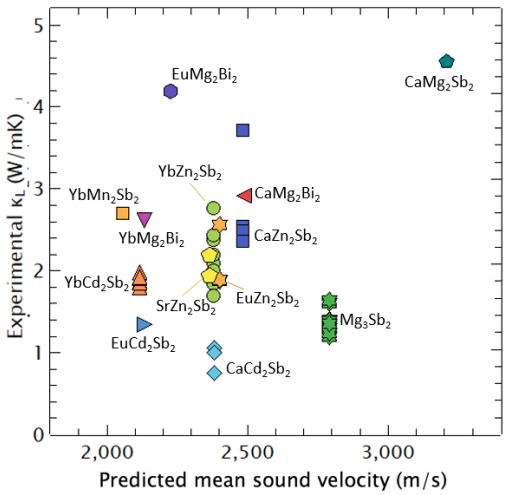


**Fig. 9** Experimental lattice thermal conductivity, $\kappa_L$, of non-alloyed samples or doped samples with less than 5% substitutions. The mean speed of sound was estimated using the calculated elastic moduli from MaterialsProject.org [139] and the experimental densities. Source data and details of the data analysis can be found in the ESI Table 5. The low $\kappa_L$ in $Mg_3Sb_2$ is surprising given its stiff bonds and light molar mass, both of which would typically be expected to lead to high thermal conductivity. [9,16,17,20,37–40,43,47–49,128,131,132,138,140–142].

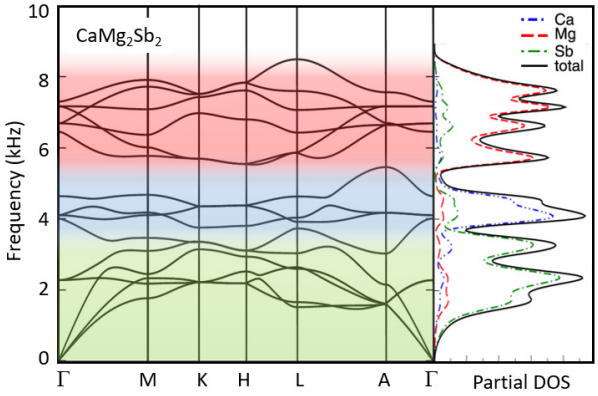


**Fig. 10** The phonon dispersion and partial phonon density of states of $CaMg_2Sb_2$ adapted from Ref. [115]. The dispersion consists of three acoustic branches and 12 optical branches. The acoustic modes are dominated by the Sb vibrational contribution, while the Ca and Mg contributions are found at high frequencies.

### 8.1 Lattice thermal conductivity reduction

Alloying with isoelectronic species on either the $A$ site or the $M$ site has been the strategy of choice to suppress the lattice thermal conductivity (e.g., $Ca_{1-x}Eu_xZn_2Sb_2$ [47], $Yb_xEu_{1-x}Cd_2Sb_2$ [9], $YbCd_{2-x}Zn_xSb_2$ [16], $YbZn_{2-x}Mn_xSb_2$ [39], $Eu(Zn_{1-x}Cd_x)_2Sb_2$ [9]). Nano-structuring has been attempted in some cases [143], but has not yet brought significant reduction in lattice thermal conductivity or improvement figure of merit $zT$. Alloying, in contrast, has been extremely successful in improving the $zT$ in $AM_2X_2$ compounds, as the reduction in lattice thermal conductivity usually far outweighs any reduction in electronic mobility. In the study by Gascoin et al. for example, the cation site of $Yb_{1-x}Ca_xZn_2Sb_2$ was systematically varied, leading to minimized $\kappa_L$ when $x = 0.5$, while the mobility remained mostly unchanged [20]. In the study of $(Eu_{0.5}Yb_{0.5})_{1-x}Ca_xMg_2Bi_2$ [17], a record high $zT$ (for $p$-type compounds) of 1.3 was achieved at 873 K for $x = 0.6$. Although the lattice thermal conductivity is typically minimized at 50% alloying, the maximum $zT$ does not always occurs at the same composition. This highlights one of the main challenges with this approach - alloying is almost always used to simultaneously optimize the carrier concentration and to create the maximum degree of point defect scattering, but these two effects rarely converge at the same composition.

This is illustrated in Fig. 11 for the alloy $YbCd_{2-x}Zn_xSb_2$ [16]. The carrier concentration varies nearly monotonically across this solid solution, with $YbCd_2Sb_2$ having $n_H = 4 \times 10^{19}$ cm$^{-3}$, and $YbZn_2Sb_2$ having $n_H = 1.15 \times 10^{20}$ cm$^{-3}$. The dependence of the mobility and lattice thermal conductivity on $n_H$, shown in Fig. 11a), clearly shows the overall benefit of alloying: the lattice thermal conductivity is significantly reduced, while the mobility is not strongly effected. For a given composition and temperature, the optimal carrier concentration can be predicted using an effective mass model by inputting the initial values of the transport properties (Seebeck coefficient, mobility, Lorenz number, lattice thermal conductivity) [134]. The solid line in Fig. 11 b) was obtained for $YbZn_2Sb_2$ using $m^* = 0.58$ m$_e$, $\mu = 86$ $cm^2/Vs$ and $\kappa_L = 0.8$ W/mk. The upper dashed line corresponds to $YbCd_2Sb_2$ with $m* = 0.75$ $m_e$, $\mu = 54$ $cm^2/Vs$ and $\kappa_L = 0.69$ W/mK. In both cases, the acoustic phonon scattering assumption is used. The experimental $zT$ of $YbCd_{2-x}Zn_xSb_2$, shown as the red symbols, is higher for alloyed compositions than the trends predicted for either of the end-members, due to the parabolic-like decrease of $\kappa_L$. We can see that the optimal composition for point defect scattering ($x \sim 1.0$) does not correspond to the optimal carrier concentration predicted within an effective mass model. Indeed, to achieve the highest possible $zT$ in this system, alloying would have to be combined with an independent approach to tuning the Fermi level.

### 8.2 Improved mobility

In general, electronic mobility in high temperature semiconductors is limited by acoustic phonon scattering - an effect that is present even in perfect single crystals (i.e., Fig. 8c). Many Zintl phases however, including the $AM_2X_2$ compounds, suffer from very low $zT$ at room temperature due to scattering mechanisms that lead to thermally-activated mobility in this temperature range. Several promising approaches have been used to improve the room temperature mobility, and thus improve the average $zT$. A recent study of $Mg_{3.1}Nb_{0.1}Sb_{1.5}Bi_{0.49}Te_{0.01}$ by Shuai et al. shows that co-doping of Nb and Te enhances the Hall mobility, leading to a 3-fold increase of the power factor at room temperature compared to that of $Mg_{3.2}Sb_{1.5}Bi_{0.49}Te_{0.01}$ [142]. The improvement was attributed to reduced ionized impurity scattering with increasing Nb content, although the mechanism is not fully understood. Grain boundaries are another likely culprit for low mobility. Kuo et al. have developed a model for the thermally-activated mobility in $Mg_3Sb_2$ that treats the grain boundaries as a separate phase with a band offset [112]. Compared with conven-

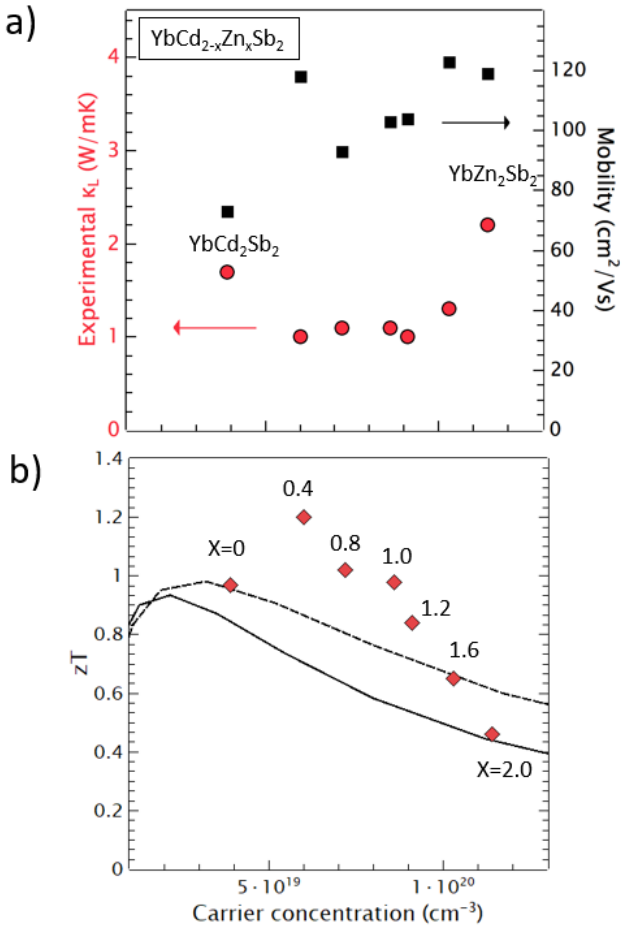


**Fig. 11** a) Alloying of $YbCd_{2-x}Zn_xSb_2$ leads to reduced $\kappa_L$, but has little influence on the mobility, $\mu_H$. b) The solid and dashed curves show the predicted carrier concentration dependence of the $zT$ for the two end member compounds, $YbZn_2Sb_2$ and $YbCd_2Sb_2$. The experimental results, shown as the red diamonds, deviate from these curves due to the effect of alloying on $\kappa_L$ [16]. Higher $zT$ values could be achieved in this system by decreasing the carrier concentration of the samples with $x \sim 1.0$ to approximately $3 \times 10^{19}$cm$^{-3}$. Note that $\mu_H$, $\kappa_L$, and carrier concentration were measured at room temperature. For the purpose of modeling the high-temperature $zT$ values, we assume the carrier concentration is temperature independent.

tional models which used Matthiesen's rule to fit the temperature dependent mobility, the two phase approach is able to better describe the experimental relationship between the Seebeck coefficients and conductivity. Samples with larger grains can be used to increase the mobility and therefore increase the integrated $zT$, opening a potential path to increase the integrated $zT$ in a number of other Zintl phases.

## 9 Opportunities and outlook

A great deal of work has been directed at understanding and optimizing the thermoelectric properties of $AM_2X_2$ compounds in the past decade, yet there are still clear gaps that remain to be filled. The thermoelectric properties of many compositions remain completely unexplored. This includes almost all arsenides and phosphides, as well as compounds with monovalent and trivalent cations and those with mixed occupancy of different valence states. In general, we have only touched the surface regarding the chemical diversity and tunability of the $CaAl_2Si_2$ structure type. Another missing piece of the puzzle is an understanding of the anisotropic properties inherent to this layered structure type. Some compounds exhibit carrier pockets that are quite anisotropic, and the dependence of this anisotropy on chemistry has not been explored. Further, the intrinsically high mobility exhibited by the rare-earth containing compounds shows that controlling the deformation potential may provide an opportunity to drastically increase the mobility in other compounds. In a similar vein, controlling the phonon-phonon scattering by studying the composition-dependence of bonding anharmonicity may lead to further reduced $\kappa_L$. The surprising $n$-type $Mg_3Sb_2$ results from Tamaki et al. and the improved understanding of how to avoid acceptor defects by controlling synthesis conditions, represent an exciting milestone. Extending these lessons to $n$-type doping of other compounds with the $CaAl_2Si_2$ structure type is a major opportunity, and employing defect calculations to identify dopants and to optimize the synthesis conditions will likely pave the way for progress in this area.

## References


1 F. J. DiSalvo, *Science*, 1999, **285**, 703–706.
2 G. J. Snyder and E. S. Toberer, *Nat. Mater.*, 2008, **7**, 105–114.
3 Y. Pei, X. Shi, A. LaLonde, H. Wang, L. Chen and G. J. Snyder, *Nature*, 2011, **473**, 66–69.
4 C. W. Li, J. Hong, A. F. May, D. Bansal, S. Chi, T. Hong, G. Ehlers and O. Delaire, *Nat. Phys.*, 2015, **11**, 1063–1069.
5 E. S. Toberer, A. F. May and G. J. Snyder, *Chem. Mater.*, 2010, **22**, 624–634.
6 S. M. Kauzlarich, *Chemistry, Structure, and Bonding of Zintl Phases and Ions*, Wiley-VCH, 1996.
7 Y. Hu and S. M. Kauzlarich, *Dalton Trans.*, 2017, **46**, 3996–4003.
8 S. Ohno, U. Aydemir, M. Amsler, J.-H. Pöhls, S. Chanakian, A. Zevalkink, M. A. White, S. K. Bux, C. Wolverton and G. J. Snyder, *Adv. Funct. Mater.*, 2017, **27**, year.
9 H. Zhang, M. Baitinger, M.-B. Tang, Z.-Y. Man, H.-H. Chen, X.-X. Yang, Y. Liu, L. Chen, Y. Grin and J.-T. Zhao, *Dalton Trans.*, 2010, **39**, 1101–1104.
10 Q. Feng Shi, Y. Li Yan and Y. Xu Wang, *Appl. Phys. Lett.*, 2014, **104**, 012104.
11 A. Zevalkink, W. G. Zeier, G. Pomrehn, E. Schechtel, W. Tremel and G. J. Snyder, *Energy Environ. Sci*, 2012, **5**, 9121–9128.
12 B. R. Ortiz, P. Gorai, V. Stevanovic and E. S. Toberer, *Chem. Mater.*, 2017.
13 J. Paik, E. Brandon, T. Caillat, R. Ewell and J.-P. Fleurial, 2011.
14 H. Tamaki, H. K. Sato and T. Kanno, *Adv. Mater.*, 2016, **28**, 10182–10187.
15 J. Zhang, L. Song, A. Mamakhel, M. R. V. Joergensen and B. B. Iversen, *Chem. Mater.*, 2017.

16 X.-J. Wang, M.-B. Tang, H.-H. Chen, X.-X. Yang, J.-T. Zhao, U. Burkhardt and Y. Grin, *Appl. Phys. Lett.*, 2009, **94**, 092106.

17 J. Shuai, H. Geng, Y. Lan, Z. Zhu, C. Wang, Z. Liu, J. Bao, C.-W. Chu, J. Sui and Z. Ren, *Proc. Natl. Acad. Sci. U.S.A.*, 2016, 201608794.

18 A. Bhardwaj and D. Misra, *RSC Adv.*, 2014, **4**, 34552–34560.

19 A. Zevalkink, W. G. Zeier, E. Cheng, J. Snyder, J.-P. Fleurial and S. Bux, *Chem. Mater.*, 2014, **26**, 5710–5717.

20 F. Gascoin, S. Ottensmann, D. Stark, S. M. Haïle and G. J. Snyder, *Adv. Funct. Mater.*, 2005, **15**, 1860–1864.

21 C. Zheng, R. Hoffmann, R. Nesper and H. G. Von Schnering, *J. Am. Chem. Soc.*, 1986, **108**, 1876–1884.

22 G. Cordier and H. Schäfer, *Z. Naturforsch. B Chem. Sci.*, 1976, **31**, 1459–1461.

23 J. Shuai, J. Mao, S. Song, Q. Zhang, G. Chen and Z. Ren, *Materials Today Phys.*, 2017, **1**, 74–95.

24 E. I. Gladyshevskii, P. I. Kipyakevich and . I. U. F. Z. Bodak, *Dalton Trans.*, 1967, 447–453.

25 E. Zintl and E. Husemann, *Z. Phys. Chem.*, 1933, **21**, 138–155.

26 A. Mewis, *Z. Naturforsch. B*, 1978, **33**, 382–384.

27 A. Mewis, *Z. Naturforsch. B*, 1978, **33**, 606–609.

28 P. Klufers and A. Mewis, *Z. Naturforsch. B*, 1977, **32**, 753–756.

29 P. Klüfers and A. Mewis, *Z. Naturforsch. B*, 1978, **33**, 151–155.

30 P. Klüfers and A. Mewis, *Z. Kristallog. Cryst. Mater.*, 1984, **169**, 135–148.

31 P. Klüfers, H. Neumann, A. Mewis and H.-U. Schuster, *Z. Naturforsch. B Chem. Sci.*, 1980, **35**, 1317–1318.

32 P. Klüfers, A. Mewis and H.-U. Schuster, *Z. Kristallog. Cryst. Mater.*, 1979, **149**, 211–226.

33 F. Wartenberg, C. Kranenberg, R. Pocha, D. Johrendt, A. Mewis, R.-D. Hoffmann, B. D. Mosel and R. Poettgen, *Z. Naturforsch. B Chem. Sci.*, 2002, **57**, 1270–1276.

34 O. Y. Zelinska, A. Tkachuk, A. Grosvenor and A. Mar, *Chem. of Metals and Alloys*, 2008, 204–209.

35 J. K. Burdett and G. J. Miller, *Chem. Mater.*, 1990, **2**, 12–26.

36 C. Zheng and R. Hoffmann, *J. Solid State Chem.*, 1988, **72**, 58–71.

37 K. Guo, Q.-G. Cao, X.-J. Feng, M.-B. Tang, H.-H. Chen, X. Guo, L. Chen, Y. Grin and J.-T. Zhao, *Eur. J. Inorg. Chem.*, 2011, **2011**, 4043–4048.

38 Q.-G. Cao, H. Zhang, M.-B. Tang, H.-H. Chen, X.-X. Yang, Y. Grin and J.-T. Zhao, *J. Appl. Phys.*, 2010, **107**, 053714.

39 C. Yu, T. Zhu, S. Zhang, X. Zhao, J. He, Z. Su and T. M. Tritt, *J. Appl. Phys.*, 2008, **104**, 013705.

40 E. S. Toberer, A. F. May, B. C. Melot, E. Flage-Larsen and G. J. Snyder, *Dalton Trans.*, 2010, **39**, 1046–54.

41 E. S. Toberer, A. Zevalkink, N. Crisosto and G. J. Snyder, *Advanced Functional Materials*, 2010, **20**, 4375–4380.

42 Z. Jiawei, S. Lirong, M. Georg K.H., F. Karl F.F., Z. Wenqing, S. Xun and I. Bo B., *Nat. Commun.*, 2016, **7**, 10892.

43 A. Zevalkink, W. G. Zeier, E. Cheng, G. J. Snyder, J.-P. Fleurial and S. Bux, *Chem. Mater.*, 2014, **26**, 5710–5717.

44 K. Imasato, S. D. Kang, S. Ohno and G. J. Snyder, *Mater. Horizons*, 2017.

45 X. Zhang, K. Peng, L. Guo, Y. Yan, H. Zhan, X. Lu, H. Gu and X. Zhou, *J. Electron. Mater.*, 2017, **46**, 2611–2615.

46 V. Ponnambalam and D. T. Morelli, *J. Electron. Mater.*, 2014, **43**, 1875–1880.

47 T. A. Wubieneh, P.-C. Wei, C.-C. Yeh, S.-y. Chen and Y.-Y. Chen, *J. Electron. Mater.*, 2016, **45**, 1942–1946.

48 J. Shuai, Y. Wang, Z. Liu, H. S. Kim, J. Mao, J. Sui and Z. Ren, *Nano Energy*, 2016, **25**, 136–144.

49 K. Guo, Q. Cao and J. Zhao, *J. Rare Earths*, 2013, **31**, 1029–1038.

50 K. Deller and B. Eisenmann, *Z. Naturforsch. B Chem. Sci.*, 1977, **32**, 612–616.

51 E. Gladyshevskii, P. Kripyakevich and O. Bodak, *Ukr. J. Phys*, 1967, **12**, 447–452.

52 C. Kranenberg, D. Johrendt and A. Mewis, *Solid State Sci.*, 2002, **4**, 261–265.

53 J. Prakash, M. C. Schäfer and S. Bobev, *Acta Cryst. C*, 2015, **71**, 894–899.

54 S. Stoyko, K. Ramachandran, P. E. Blanchard, K. A. Rosmus, J. A. Aitken and A. Mar, *J. Solid State Chem.*, 2014, **213**, 275–286.

55 M. Khatun, S. S. Stoyko and A. Mar, *Inorg. Chem.*, 2013, **52**, 3148–3158.

56 X. Lai, X. Chen, S. Jin, G. Wang, T. Zhou, T. Ying, H. Zhang, S. Shen and W. Wang, *Inorg. Chem.*, 2013, **52**, 12860–12862.

57 J. Evers, *Zintl Phases: Principles and Recent Developments*, Springer Science & Business Media, 2011, vol. 139.

58 D. Bende, Y. Grin and F. R. Wagner, *Chem. A Eur. J.*, 2014, **20**, 9702–9708.

59 D. Bende, F. R. Wagner and Y. Grin, *Inorg. Chem.*, 2015, **54**, 3970–3978.

60 C. Kranenberg, D. Johrendt and A. Mewis, *Z. Anorg. Allg. Chem*, 1999, **625**, 1787–1793.

61 D. Ramirez, A. Gallagher, R. Baumbach and T. Siegrist, *J. Solid State Chem.*, 2015, **231**, 217–222.

62 P. Alemany, M. Llunell and E. Canadell, *J. Comput. Chem.*, 2008, **29**, 2144–2153.

63 M. Khatun, S. S. Stoyko and A. Mar, *Inorg. Chem.*, 2013, **52**, 3148–58.

64 I. Grund, H.-U. Schuster and P. Müller, *Z. Anorg. Allg. Chem*, 1984, **515**, 151–158.

65 E. Jang, G. Nam, H. Woo, J. Lee, M. Han, S. Kim and T. You, *Eur. J. Inorg. Chem.*, 2015, **2015**, 2786–2793.

66 M. C. Schäfer, N.-T. Suen, M. Raglione and S. Bobev, *J. Solid State Chem.*, 2014, **210**, 89–95.

67 E. Brechtel, G. Cordier and H. Schäfer, *Z. Naturforsch. B*, 1978, **33**, 820–822.

68 E. Brechtel, G. Cordier and H. Schäfer, *Z. Naturforsch. B*, 1979, **34**, 921–925.

69 R. Rühl and W. Jeitschko, *Mater. Res. Bull.*, 1979, **14**, 513–517.

70 I. Schellenberg, M. Eul, W. Hermes and R. Pöttgen, *Z. Anorg. Allg. Chem*, 2010, **636**, 85–93.

71 A. Morozkin, O. Isnard, P. Henry, S. Granovsky, R. Nirmala and P. Manfrinetti, *J. Alloys Compd.*, 2006, **420**, 34–36.

72 G. Zwiener, H. Neumann and H.-U. Schuster, *Z. Naturforsch. B Chem. Sci.*, 1981, **36**, 1195–1197.

73 A. Nateprov, J. Cisowski, J. Heimann and I. Mirebeau, *J. Alloys Compd.*, 1999, **290**, 6–9.

74 A. Artmann, A. Mewis, M. Roepke and G. Michels, *Z. Anorg. Allg. Chem*, 1996, **622**, 679–682.

75 R. Juza and R. Kroebel, *Z. Anorg. Allg. Chem*, 1964, **331**, 187–199.

76 M. Martinez-Ripoll, A. Haase and G. Brauer, *Acta Cryst. Section B: Structural Crystall. and Crystal Chem.*, 1974, **30**, 2006–2009.

77 A. F. May, M. A. McGuire, D. J. Singh, R. Custelcean and G. E. Jellison Jr., *Inorg. Chem.*, 2011, **50**, 11127–11133.

78 A. Murav'eva, O. Zarechnyuk and E. Gladyshevskii, *Systems Y–Al–Si (Ge, Sb) in the range 0 tO 33.3 at. percent Y.*, Lvov state univ. technical report, 1971.

79 R. Xesper and H. G. v. Schnering, *Z. Naturforsch. B Chem. Sci.*, 1982, **37**, 1514–1517.

80 C. Kranenberg, D. Johrendt, A. Mewis, R. Pöttgen, G. Kotzyba, C. Rosenhahn and B. D. Mosel, *Solid State Sci.*, 2000, **2**, 215–222.

81 N. Muts, R. Gladyshevskii and E. Gladyshevskii, *J. Alloys Compd.*, 2005, **402**, 66–69.

82 S. Andersen, C. Marioara, A. Frøseth, R. Vissers and H. Zandbergen, *Mater. Sci. Eng. A*, 2005, **390**, 127–138.

83 P. Schobinger-Papamantellos and F. Hulliger, *J. Less Common Met.*, 1989, **146**, 327–335.

84 H. Flandorfer, D. Kaczorowski, J. Gröbner, P. Rogl, R. Wouters, C. Godart and A. Kostikas, *J. Solid State Chem.*, 1998, **137**, 191–205.

85 O. Reckeweg and F. J. DiSalvo, *Z. Anorg. Allg. Chem*, 2001, **627**, 371–377.

86 G. Nolas, J. Yang and R. Ertenberg, *Phys. Rev. B*, 2003, **68**, 193206.

87 Y. Qin, P. Qiu, R. Liu, Y. Li, F. Hao, T. Zhang, D. Ren, X. Shi and L. Chen, *J. Mater. Chem.*, 2016, **4**, 1277–1289.

88 R. Pöttgen and D. Johrendt, *Intermetallics: synthesis, structure, function*, Walter de Gruyter GmbH & Co KG, 2014.

89 K. Kihou, H. Nishiate, A. Yamamoto and C.-H. Lee, *Inorganic Chemistry*, 2017, **56**, 3709–3712.

90 J. E. Iglesia, K. E. Pachali and H. J. Steinfink, *Solid State Chem.*, 1974, **9**, 6–14.

91 C. L. Condron, H. Hope, P. M. B. Piccoli, A. J. Schultz and S. M. Kauzlarich, *Inorg. Chem.*, 2007, **46**, 4523–4529.

92 W. B. Pearson, *A handbook of lattice spacings and structures of metals and alloys: International series of monographs on metal physics and physical metallurgy*, Elsevier, 2013, vol. 4.

93 R. Hoffmann and C. Zheng, *J. Phys. Chem.*, 1985, **89**, 4175–4181.

94 D. Mandrus, A. S. Sefat, M. A. McGuire and B. C. Sales, *Chem. Mater.*, 2010, **22**, 715–723.

95 B. Saparov and A. S. Sefat, *J. Solid State Chem.*, 2013, **204**, 32–39.

96 Z. Xiao, H. Hiramatsu, S. Ueda, Y. Toda, F.-Y. Ran, J. Guo, H. Lei, S. Matsuishi, H. Hosono and T. Kamiya, *J. Am. Chem. Soc.*, 2014, **136**, 14959–14965.

97 J. C. Slater, *J. Chem. Phys.*, 1964, **41**, 3199–3204.

98 S. Leoni, W. Carrillo-Cabrera, W. Schnelle and Y. Grin, *Solid State Sci.*, 2003, **5**, 139–148.

99 A. Zevalkink, M. Bobnar, U. Schwarz and Y. Grin, *Chem. Mater.*, 2016.

100 S. Yamanaka, M. Kajiyama, S. N. Sivakumar and H. Fukuoka, *High Pressure Research*, 2004, **24**, 481–490.

101 C. T. Prewitt and R. T. Downs, *Rev. in Mineralogy*, 1998, **37**, 284–318.

102 S. Bobev, P. H. Tobash, V. Fritsch, J. D. Thompson, M. F. Hundley, J. L. Sarrao and Z. Fisk, *J. Solid State Chem.*, 2005, **178**, 2091–2103.

103 A. F. May, M. A. McGuire, D. J. Singh, J. Ma, O. Delaire, A. Huq, W. Cai and H. Wang, *Phys. Rev. B*, 2012, **85**, 035202.

104 M. Imai, H. Abe and K. Yamada, *Inorg. Chem.*, 2004, **43**, 5186–5188.

105 S. H. Kim, C. M. Kim, Y.-K. Hong, K. I. Sim, J. H. Kim, T. Onimaru, T. Takabatake and M.-H. Jung, *Materials Research Express*, 2015, **2**, 055903.

106 S. Kim, C. Kim, Y.-K. Hong, T. Onimaru, K. Suekuni, T. Takabatake and M.-H. Jung, *J. Mater. Chem. A*, 2014, **2**, 12311–12316.

107 H. Zhang, J. Zhao, Y. Grin, X. Wang, M. Tang, Z. Man, H. Chen and X. Yang, *J. Chem. Phys.*, 2008, **129**, 164713.

108 V. Ponnambalam and D. T. Morelli, *J. Electron. Mater.*, 2013, **42**, 1307.

109 Y. Takagiwa, Y. Sato, A. Zevalkink, I. Kanazawa, K. Kimura, Y. Isoda and Y. Shinohara, *J Alloys Compd.*, 2017, **703**, 73–79.

110 J. Zhang, L. Song, S. H. Pedersen, H. Yin, L. T. Hung and B. B. Iversen, *Nat. Commun.*, 2017, **8**, 13901.

111 S. Ohno, K. Imasato, S. Anand, H. Tamaki, S. D. Kang, P. Gorai, H. K. Sato, E. S. Toberer, T. Kanno and G. J. Snyder, *Joule*, 2017, **2**, year.

112 J. J. Kuo, S. D. Kang, K. Imasato, H. Tamaki, S. Ohno, T. Kanno and G. J. Snyder, *Energy Environ. Sci.*, 2018.

113 A. Zunger, *Appl. Phys. Lett.*, 2003, **83**, 57–59.

114 G. Ceder and K. Persson, *The Materials Project: A Materials Genome Approach*, 2010.

115 D. J. Singh and D. Parker, *J. Appl. Phys.*, 2013, **114**, 143703.

116 W. G. Zeier, A. Zevalkink, Z. M. Gibbs, G. Hautier, M. G. Kanatzidis and G. J. Snyder, *Angew. Chem. Int. Ed.*, 2016, **55**, 6826–6841.

117 P. A. Cox, *The electronic structure and chemistry of solids*, Ox-

ford Univ. Press Oxford etc., 1987.
118 O. Reckeweg, C. Lind, A. Simon and F. J. DiSalvo, *Z. Naturforsch. B Chem. Sci.*, 2003, **58**, 159–162.
119 Y.-K. Kuo, K. Sivakumar, J. Tasi, C. S. Lue, J. Huang, S. Wang, D. Varshney, N. Kaurav and R. Singh, *J. Phys. Condens. Matter*, 2007, **19**, 176206.
120 C. Lue, C. Fang, A. Abhyankar, J. Lin, H. Lee, C. Chang and Y. Kuo, *Intermetallics*, 2011, **19**, 1448–1454.
121 T. Pandey and A. K. Singh, *Phys. Chem. Chem. Phys.*, 2015, **17**, 16917–16926.
122 F. Tran and P. Blaha, *Phys. Rev. Lett.*, 2009, **102**, 226401.
123 D. J. Singh, *Phys. Rev. B*, 2010, **82**, 205102.
124 G. S. Pomrehn, A. Zevalkink, W. G. Zeier, A. van de Walle and G. J. Snyder, *Angew. Chem. Int. Ed. Engl.*, 2014, **53**, 3422–6.
125 K. Imasato, S. D. Kang, S. Ohno and G. J. Snyder, *Mater. Horizons*, 2018.
126 J. Zhang, L. Song, G. K. Madsen, K. F. Fischer, W. Zhang, X. Shi and B. B. Iversen, *Nat. Commun.*, 2016, **7**, 10892.
127 G. Huang, M. Liu, L. Chen and D. Xing, *J. Phys. Condens. Matter*, 2005, **17**, 7151.
128 J. Zhang, L. Song, S. H. Pedersen, H. Yin, L. T. Hung and B. B. Iversen, *Nat. Comm.*, 2017, **8**, 13901.
129 G. Mahan and J. Sofo, *Proc. Natl. Acad. Sci. U.S.A.*, 1996, **93**, 7436–7439.
130 L. Song, J. Zhang and B. B. Iversen, *J. Mater. Chem.*, 2017, **5**, 4932–4939.
131 J. Shuai, Y. Wang, H. S. Kim, Z. Liu, J. Sun, S. Chen, J. Sui and Z. Ren, *Acta Mater.*, 2015, **93**, 187–193.
132 A. Bhardwaj, A. Rajput, A. Shukla, J. Pulikkotil, A. Srivastava, A. Dhar, G. Gupta, S. Auluck, D. Misra and R. Budhani, *RSC Adv.*, 2013, **3**, 8504–8516.
133 L. Bjerg, G. K. Madsen and B. B. Iversen, *Chem. Mater.*, 2012, **24**, 2111–2116.
134 A. May and G. Snyder, *Materials, preparation, and characterization in thermoelectrics. CRC Press, Boca Raton*, 2012, **11**,.
135 A. F. May, M. A. McGuire, J. Ma, O. Delaire, A. Huq and R. Custelcean, *J. Appl. Phys.*, 2012, **111**, 033708.
136 J. Shuai, Z. Liu, H. S. Kim, Y. Wang, J. Mao, R. He, J. Sui and Z. Ren, *J. Mater. Chem. A*, 2016, **4**, 4312–4320.
137 E. S. Toberer, A. Zevalkink and G. J. Snyder, *J. Mater. Chem.*, 2011, **21**, 15843–15852.
138 M. Wood, S. Ohno, U. Aydemir and G. J. Snyder, 2018.
139 M. De Jong, W. Chen, T. Angsten, A. Jain, R. Notestine, A. Gamst, M. Sluiter, C. K. Ande, S. Van Der Zwaag, J. J. Plata *et al.*, *Sci. Data*, 2015, **2**, 150009.
140 H. Zhang, L. Fang, M. Tang, H. Chen, X. Yang, X. Guo, J. Zhao and Y. Grin, *Intermetallics*, 2010, **18**, 193–198.
141 J. Shuai, H. S. Kim, Z. Liu, R. He, J. Sui and Z. Ren, *Appl. Phys. Lett.*, 2016, **108**, 183901.
142 J. Shuai, J. Mao, S. Song, Q. Zhu, J. Sun, Y. Wang, R. He, J. Zhou, G. Chen, D. J. Singh *et al.*, *Energy Environ. Sci.*, 2017, **10**, 799–807.
143 X. Zhang, B. Zhang, K.-l. Peng, X.-c. Shen, G.-t. Wu, Y.-c. Yan, S.-j. Luo, X. Lu, G.-y. Wang, H.-s. Gu *et al.*, *Nano Energy*, 2018, **43**, 159–167.